



# GOALS-JWST: NIRC*am* and MIRI Imaging of the Circumnuclear Starburst Ring in NGC 7469

Thomas Bohn<sup>1</sup> , Hanae Inami<sup>1</sup> , Tanio Diaz-Santos<sup>2,3</sup> , Lee Armus<sup>4</sup> , S. T. Linden<sup>5</sup> , Vivian U<sup>6</sup> , Jason Surace<sup>4</sup> , Kirsten L. Larson<sup>7</sup> , Aaron S. Evans<sup>8,9</sup> , Shunshi Hoshioka<sup>1</sup>, Thomas Lai<sup>4</sup> , Yiqing Song<sup>8,9</sup> , Joseph M. Mazzarella<sup>4</sup> , Loreto Barcos-Munoz<sup>8,9</sup> , Vassilis Charmandaris<sup>2,3,10</sup> , Justin H. Howell<sup>4</sup> , Anne M. Medling<sup>11,12</sup> , George C. Privon<sup>8,13</sup> , Jeffrey A. Rich<sup>14</sup> , Sabrina Stierwalt<sup>15</sup> , Susanne Aalto<sup>16</sup> , Torsten Böker<sup>17</sup> , Michael J. I. Brown<sup>18</sup> , Kazushi Iwasawa<sup>19,20</sup> , Matthew A. Malkan<sup>21</sup> , Paul P. van der Werf<sup>22</sup> , Philip Appleton<sup>4</sup> , Christopher C. Hayward<sup>23</sup> , Francisca Kemper<sup>20,24,25</sup> , David Law<sup>26</sup> , Jason Marshall<sup>27</sup> , Eric J. Murphy<sup>8</sup> , and David Sanders<sup>28</sup>

<sup>1</sup> Hiroshima Astrophysical Science Center, Hiroshima University, 1-3-1 Kagamiyama, Higashi-Hiroshima, Hiroshima 739-8526, Japan; [tbohn002@ucr.edu](mailto:tbohn002@ucr.edu)

<sup>2</sup> Institute of Astrophysics, Foundation for Research and Technology-Hellas (FORTH), Heraklion, 70013, Greece

<sup>3</sup> School of Sciences, European University Cyprus, Diogenes street, Engomi, 1516 Nicosia, Cyprus

<sup>4</sup> IPAC, California Institute of Technology, 1200 E. California Blvd., Pasadena, CA 91125, USA

<sup>5</sup> Department of Astronomy, University of Massachusetts at Amherst, Amherst, MA 01003, USA

<sup>6</sup> Department of Physics and Astronomy, 4129 Frederick Reines Hall, University of California, Irvine, CA 92697, USA

<sup>7</sup> AURA for the European Space Agency (ESA), Space Telescope Science Institute, 3700 San Martin Drive, Baltimore, MD 21218, USA

<sup>8</sup> National Radio Astronomy Observatory, 520 Edgemont Road, Charlottesville, VA 22903, USA

<sup>9</sup> Department of Astronomy, University of Virginia, 530 McCormick Road, Charlottesville, VA 22903, USA

<sup>10</sup> Department of Physics, University of Crete, Heraklion, 71003, Greece

<sup>11</sup> Department of Physics & Astronomy and Ritter Astrophysical Research Center, University of Toledo, Toledo, OH 43606, USA

<sup>12</sup> ARC Centre of Excellence for All Sky Astrophysics in 3 Dimensions (ASTRO 3D); Australia

<sup>13</sup> Department of Astronomy, University of Florida, P.O. Box 112055, Gainesville, FL 32611, USA

<sup>14</sup> The Observatories of the Carnegie Institution for Science, 813 Santa Barbara Street, Pasadena, CA 91101, USA

<sup>15</sup> Occidental College, Physics Department, 1600 Campus Road, Los Angeles, CA 90042, USA

<sup>16</sup> Department of Space, Earth and Environment, Chalmers University of Technology, SE-412 96 Gothenburg, Sweden

<sup>17</sup> European Space Agency, Space Telescope Science Institute, Baltimore, MD 21218, USA

<sup>18</sup> School of Physics & Astronomy, Monash University, Clayton, VIC 3800, Australia

<sup>19</sup> Institut de Ciències del Cosmos (ICCUB), Universitat de Barcelona (IEEC-UB), Martí i Franquès, 1, E-08028 Barcelona, Spain

<sup>20</sup> ICREA, Pg. Lluís Companys 23, E-08010 Barcelona, Spain

<sup>21</sup> Department of Physics & Astronomy, UCLA, Los Angeles, CA 90095-1547, USA

<sup>22</sup> Leiden Observatory, Leiden University, PO Box 9513, 2300 RA Leiden, The Netherlands

<sup>23</sup> Center for Computational Astrophysics, Flatiron Institute, 162 Fifth Avenue, New York, NY 10010, USA

<sup>24</sup> Institut de Ciències de l'Espai (ICE, CSIC), Can Magrans, s/n, E-08193 Bellaterra, Barcelona, Spain

<sup>25</sup> Institut d'Estudis Espacials de Catalunya (IEEC), E-08034 Barcelona, Spain

<sup>26</sup> Space Telescope Science Institute, 3700 San Martin Drive, Baltimore, MD 21218, USA

<sup>27</sup> Glendale Community College, 1500 N. Verdugo Road, Glendale, CA 91208, USA

<sup>28</sup> Institute for Astronomy, University of Hawaii, 2680 Woodlawn Drive, Honolulu, HI 96822, USA

Received 2022 September 9; revised 2022 December 5; accepted 2022 December 6; published 2023 January 13

## Abstract

We present James Webb Space Telescope (JWST) imaging of NGC 7469 with the Near-Infrared Camera and the Mid-Infrared Instrument. NGC 7469 is a nearby,  $z = 0.01627$ , luminous infrared galaxy that hosts both a Seyfert Type-1.5 nucleus and a circumnuclear starburst ring with a radius of  $\sim 0.5$  kpc. The new near-infrared (NIR) JWST imaging reveals 66 star-forming regions, 37 of which were not detected by Hubble Space Telescope (HST) observations. Twenty-eight of the 37 sources have very red NIR colors that indicate obscurations up to  $A_V \sim 7$  and a contribution of at least 25% from hot dust emission to the  $4.4 \mu\text{m}$  band. Their NIR colors are also consistent with young ( $< 5$  Myr) stellar populations and more than half of them are coincident with the mid-infrared (MIR) emission peaks. These younger, dusty star-forming regions account for  $\sim 6\%$  and  $\sim 17\%$  of the total 1.5 and  $4.4 \mu\text{m}$  luminosity of the starburst ring, respectively. Thanks to JWST, we find a significant number of young dusty sources that were previously unseen due to dust extinction. The newly identified 28 young sources are a significant increase compared to the number of HST-detected young sources (4–5). This makes the total percentage of the young population rise from  $\sim 15\%$  to 48%. These results illustrate the effectiveness of JWST in identifying and characterizing previously hidden star formation in the densest star-forming environments around active galactic nuclei (AGN).

*Unified Astronomy Thesaurus concepts:* Luminous infrared galaxies (946); Infrared astronomy (786); Infrared sources (793); Star forming regions (1565)

*Supporting material:* machine-readable table

## 1. Introduction

NGC 7469 is a nearby ( $z = 0.01627$ ) luminous infrared galaxy ( $L_{\text{IR},8-1000\mu\text{m}} = 10^{11.6} L_{\odot}$ ) that is part of the Great Observatories All-sky LIRGs Survey (GOALS; Armus et al. 2009). NGC 7469 hosts both a Type-1.5 Seyfert nucleus

(Landt et al. 2008) and a compact ( $r = 0.5$  kpc) circumnuclear starburst ring (Miles et al. 1994; Genzel et al. 1995; Fathi et al. 2015; Song et al. 2021). Extensive multiband imaging and spectroscopy have been reported in the literature (e.g., Inami et al. 2013, 2018; Stierwalt et al. 2013), and its Type-1.5 nucleus is one of the most extensively studied in the sky (e.g., Behar et al. 2017; Linden et al. 2019; Larson et al. 2020). Reverberation mapping measurements indicate a black hole mass of  $\sim 10^7 M_\odot$  (Peterson et al. 2014; Lu et al. 2021) and an active galactic nucleus (AGN)-driven biconical outflow of highly ionized gas has been observed (Müller-Sánchez et al. 2011; Robledo-Orus et al. 2021; Xu & Wang 2022). Radio observations also reveal a nuclear CO molecular bar inside the ring that crosses the AGN (Davies et al. 2004; Izumi et al. 2015, 2020).

The circumnuclear starburst ring accounts for about two-thirds of the bolometric luminosity of the galaxy (Genzel et al. 1995; Song et al. 2021). Hubble Space Telescope (HST)-based UV-through-near-infrared (NIR) spectral energy distribution (SED) fitting of 30  $1.1 \mu\text{m}$ -selected star-forming regions found in the ring suggests a bimodality in the stellar population (Díaz-Santos et al. 2007, hereafter DS07). DS07 found that 19 of the regions are likely of intermediate age (8–20 Myr) and are found in regions of low extinction,  $A_V \sim 1.25$  mag. Five of the remaining regions were classified as having younger ages (1–3 Myr) and are located in regions of higher extinction,  $A_V \sim 3$  mag. This younger, obscured population coincides with the peaks in the radio free-free emission (DS07; Orienti & Prieto 2010). The intermediate-aged population, on the other hand, is responsible for the UV, optical, and NIR continuum emission.

NGC 7469 provides the unique opportunity to study the starburst-AGN connection since it hosts an AGN surrounded by a starburst ring. However, due to the compact nature of this system, it was difficult to achieve both the resolution and sensitivity needed to study the circumnuclear environment in the mid-infrared (MIR) on subkiloparsec scales. With JWST, we can now explore the dustiest regions of the starburst ring on these scales.

In this Letter, we examine NIRCам and MIRI imaging of the circumnuclear starburst ring in NGC 7469. With the unprecedented spatial resolution and sensitivity of JWST, we identify a new set of previously undetected star-forming regions that are heavily obscured by dust. A cosmology of  $H_0 = 70 \text{ km s}^{-1} \text{ Mpc}^{-1}$ ,  $\Omega_\Lambda = 0.72$ , and  $\Omega_{\text{matter}} = 0.28$  is adopted. With this cosmology, NGC 7469 is located 70.8 Mpc away, and  $1''$  subtends 330 pc.

## 2. Observations

JWST/MIRI (Bouchet et al. 2015; Rieke et al. 2015) imaging was obtained with the F560W ( $5.6 \mu\text{m}$ ), F770W ( $7.7 \mu\text{m}$ ), and F1500W ( $15.0 \mu\text{m}$ ) filters with both the BRIGHTSKY and SUB128 subarray modes. Our analysis was done on the SUB128 subarray data where the full starburst ring was observable in the field of view (FOV:  $14.''1 \times 14.''1$ ). Here, the nucleus remained unsaturated by the AGN. Observations of the SUB128 were taken on 2022 July 2, where the exposure time was 46 s for the F560W filter and 48 s for the F770W and F1500W filters. Figure 1(a) shows a false-color image of the MIRI/BRIGHTSKY subarray data.

JWST/NIRCам (Greene et al. 2016) imaging was taken with the F150W ( $1.5 \mu\text{m}$ ), F200W ( $2.0 \mu\text{m}$ ), F335M ( $3.4 \mu\text{m}$ ), and F444W ( $4.4 \mu\text{m}$ ) filters. Like MIRI, we use the SUB160P

subarray data due to the nucleus being saturated by the AGN in all of the full array images. The entire starburst ring fits within the FOV (short- $5'' \times 5''$ , long- $10'' \times 10''$ ) of the subarray mode and the nucleus was only partially saturated in the F335M and F444W filters. SUB160P observations were taken on 2022 July 3, where the exposure time for each filter was 67 s. Figure 1(b) shows a false-color image of the NIRCам/SUB160P subarray data.

All images were processed through the standard JWST reduction pipeline (Gordon et al. 2015), and we selected stage 3 calibrated images for analysis. We made corrections to the World Coordinate System coordinates to align all the NIRCам and MIRI calibrated images to the Gaia reference frame using publicly available routines.<sup>29,30</sup> Due to the contemporary state of JWST, the reduction pipeline is continuously receiving updates. As such, we have applied the most current up-to-date zero-point corrections (CRDS0989) to the flux densities in each NIRCам filter (Boyer et al. 2022).<sup>31</sup>

## 3. Analysis

Before source identification was performed, the complex point-spread function (PSF) was fit and subtracted from the central source to minimize contamination from instrumental scattered light. This was done by first fitting the AGN with a PSF model using GALFIT (Peng et al. 2010), where the PSF was constructed using the WEBBPSF simulation tool (Perrin et al. 2014).<sup>32</sup> The best-fit PSF model was then subtracted, and pixels showing excess emission within the AGN were masked.

Source identification over the starburst ring was then performed, first on the NIRCам/F150W image to take advantage of the high spatial resolution (see Figure 2). The lack of strong emission lines within its wavelength coverage makes it well suited to sample the continuum emission. To identify sources, the DAOFIND (Stetson 1987) algorithm from the PHOTUTILS detection package (Bradley et al. 2022) was used, where a detected source needed to have an FWHM greater than or equal to the PSF FWHM of the filter and a peak emission  $3\sigma$  above the local background. This results in a detection limit of  $\sim 400 \text{ MJy sr}^{-1}$ .

A total of 59 star-forming regions were detected in the starburst ring in the F150W filter. About 40 (67%) of these objects appear as unresolved sources. Because the measured FWHM of the PSF of the F150W filter, as determined by field stars, corresponds to  $\sim 22$  pc, the sizes of the unresolved sources are consistent with those of stellar clusters in nearby galaxies, making them viable candidates for compact clusters (Linden et al. 2017; Norris et al. 2019; Brown & Gnedin 2021). We do not refer to the resolved sources as compact clusters because a cluster refers to a distinct grouping of stars, which is best modeled as a single-stellar population, and are likely gravitationally bound (Krumholz et al. 2019). For consistency, we refer to all detected sources as “regions,” whether they are resolved or not. We also note that 29 of the F150W-detected sources were selected via HST/F110W ( $1.1 \mu\text{m}$ ) filter imaging in DS07. An additional source, C26, was detected in DS07 but

<sup>29</sup> <https://github.com/dancoe/NIRCам>

<sup>30</sup> [https://github.com/STScI-MIRI/Imaging\\_ExampleNB](https://github.com/STScI-MIRI/Imaging_ExampleNB)

<sup>31</sup> <https://www.stsci.edu/contents/news/jwst/2022/an-improved-nircam-flux-calibration-is-now-available>

<sup>32</sup> <https://www.stsci.edu/jwst/science-planning/proposal-planning-toolbox/psf-simulation-tool>

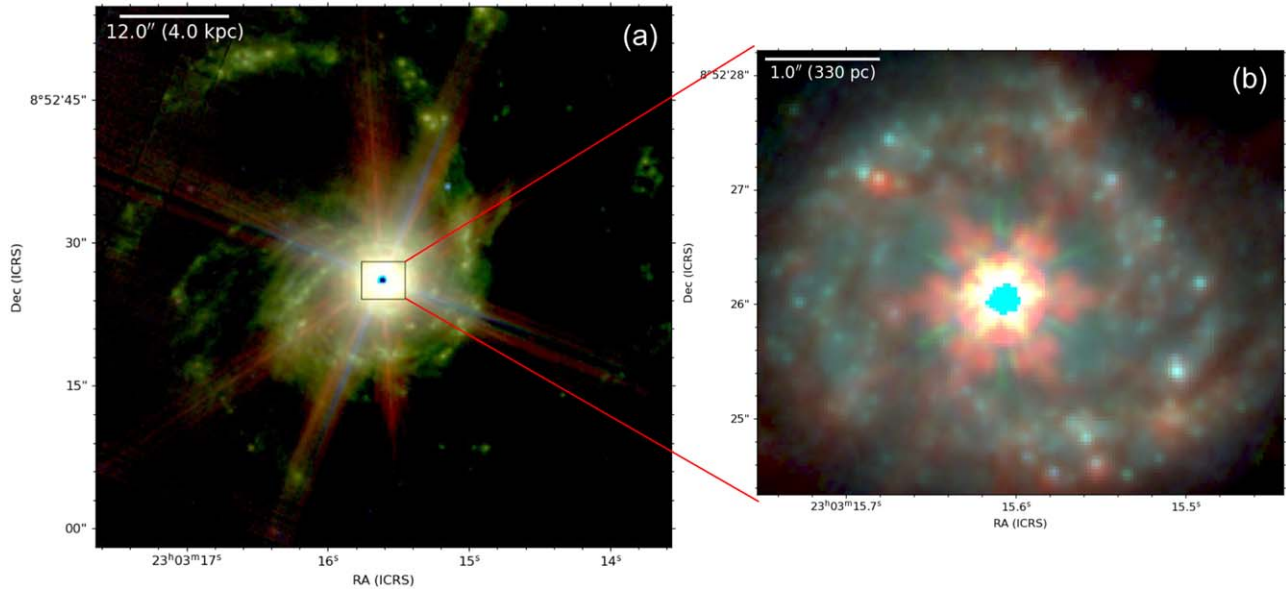


**Figure 1.** False-color images of NGC 7469 taken with MIRI/BRIGHTSKY (a) and NIRCcam/SUB160P subarray modes (b). The MIRI image contains all three observed filters: F560W (blue), F770W (green), and F1500W (red). The central box on the left represents the size of the subarray image on the right. The NIRCcam imaging includes the F150W (blue), F200W (green), and F444W (red) filters. Fifty-nine and 22 pixels are saturated in the MIRI/F1500W and NIRCcam/F444W filters, which have the most saturation, due to the central AGN, respectively. Note that the AGN is not subtracted in these images. North is up and the east is to the left.

only in the HST 1.1  $\mu\text{m}$  band. This source is not detected in the JWST images and we exclude it from the analysis.

To investigate potentially missing sources due to extreme dust obscuration, we ran a similar selection scheme on the F444W image. The F444W filter better samples the continuum than the F335M filter, which may be contaminated by the 3.3  $\mu\text{m}$  polycyclic aromatic hydrocarbon (PAH) feature. An additional seven sources were discovered this way, resulting in a total of 66 star-forming regions detected in the F150W and F444W images (see Figure 2). For sources that are not detected in a particular filter, we denote the extracted flux as an upper limit (see Table 1). Lastly, we note that two star-forming regions were detected only in the F335M filter. These are likely PAH-dominated sources and we list them in Table 1 together with the F150W and F444W-selected sources.

Due to the angular resolution differences between NIRCcam and MIRI, a separate sample of star-forming regions was identified in the MIR. Thirteen regions were found in the F560W image using the same method as used above. Of these, two regions were rejected due to intersection with the AGN diffraction spikes. The remaining 11 sources serve as our MIRI sample and their locations are shown in Figure 2.

Aperture photometry was performed using the PHOTUTILS photometry package.<sup>33</sup> For NIRCcam, the radius of the extraction aperture was set to  $0''.073$ , the largest size at which there is no source overlap in all four filters. For MIRI, the aperture radius for all three filters was set to  $0''.31$ , where source overlap was also kept to a minimum. To perform local background subtraction, background annuli with varying radii were used. The inner and outer radii ranged from 1.1 to 2.0 and 1.5 to 4.0 times the radius of each aperture, respectively. Any source overlapping with the background annuli was masked and the three sigma-clipped median of the annuli measurements was used for background subtraction (typically 30%–45% of the source flux). Following this, aperture corrections were

applied using the encircled aperture-to-total energy of each filter.<sup>34,35</sup> The resulting flux densities are listed in Table 1.

## 4. Results

The significant improvement in sensitivity of JWST over previous NIR and MIR observations is evident from the number of new sources identified. Thirty-seven star-forming regions were newly discovered with NIRCcam, with some single HST sources being resolved into two or more sources. Additionally, 11 regions are detected in the MIRI/F560W image. In the following sections, we discuss the spatial locations, colors, and estimates of the ages of this new population of star-forming regions.

### 4.1. Locations of Sources

Figure 3 displays the locations of the NIRCcam star-forming regions. Overall, the 66 detected sources are evenly distributed azimuthally throughout the ring. However, we find that the newly detected JWST sources are somewhat clustered toward the north and southwest regions, which coincide with the peaks of radio emission at the both ends of the nuclear CO molecular bar (see Section 5 for further discussion).

In the MIRI images, seven regions of strong MIR emission (M1–M6, M10) are clearly seen in the ring (see Figure 2). The locations of these regions match well with previous ground-based MIR observations of the starburst ring (Soifer et al. 2003; Ramos Almeida et al. 2011). With JWST, an additional four new regions are identified in the northwest (M7, M8, M11) and northeast (M9). The combined luminosity of these seven regions accounts for  $\sim 36\%$  of the total luminosity of the starburst ring at 5.6  $\mu\text{m}$ .

<sup>34</sup> <https://jwst-docs.stsci.edu/jwst-near-infrared-camera/nircam-performance/nircam-point-spread-functions>

<sup>35</sup> <https://jwst-docs.stsci.edu/jwst-mid-infrared-instrument/miri-performance/miri-point-spread-functions>

<sup>33</sup> <https://photutils.readthedocs.io/en/stable/aperture.html>



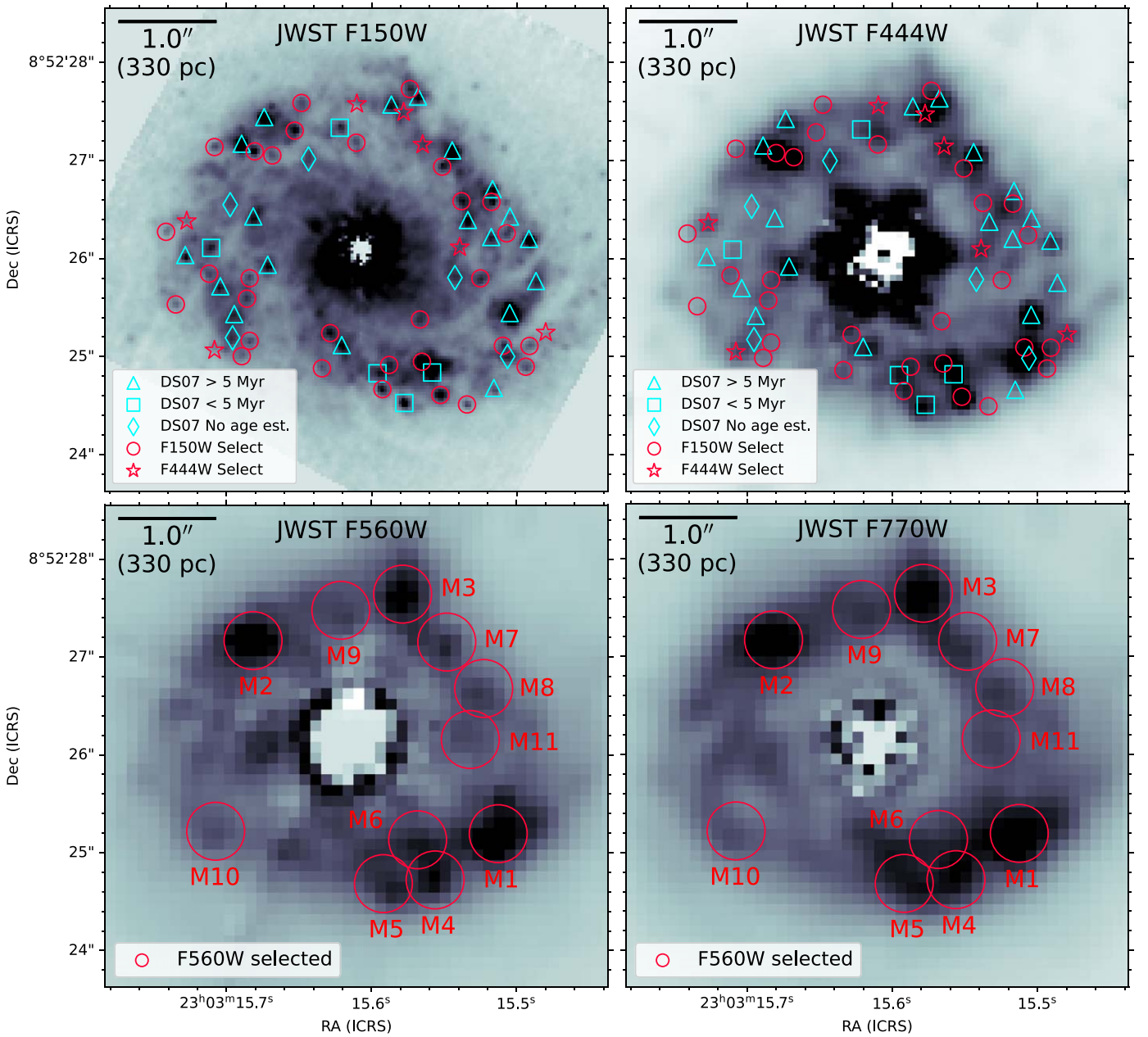


**Figure 2.** NIRCam and MIRI image mosaic of the starburst ring in four filters: NIRCam/F150W, NIRCam/F444W, MIRI/F560W, and MIRI/F770W. The AGN has been masked out in each filter. The source locations for both the NIRCam and MIRI region catalogs are overplotted. Note that the marker sizes are not representative of the extraction sizes. In the top panels, sources identified with HST at  $1.1 \mu\text{m}$  by DS07 that span a range of ages  $<5$  Myr (cyan squares) to  $>5$  Myr (cyan triangles) are shown. We also include five sources from DS07 where age estimation could not be determined (cyan diamonds). Star-forming regions newly identified with JWST are shown as red circles (F150W-selected) and stars (F444W-selected). In the bottom panels, star-forming regions identified in the F560W filter are shown as red circles and are labeled from the brightest, M1, to the faintest, M11. In total, we detect 66 star-forming regions in NIRCam. This more than doubles the 30 sources previously identified by HST.

A comparison of Figures 1(b) and 3 reveals that the sources detected by HST in DS07 tend to be the bluest and brightest sources in the F150W filter, while JWST uncovers the reddest and faintest sources. Indeed, some of the brightest regions in the F444W filter (N5, N15, N19) are not detected by HST. The brightest source at  $4.4 \mu\text{m}$  is N5, and is clearly seen as a red source in Figure 1(b). Lastly, as shown in Figure 3, over half of the newly detected NIRCam sources—the majority of which have redder colors—fall within regions of strong MIR emission.

#### 4.2. NIR Colors of Sources

Figure 4 shows the F200W/F150W flux ratios against the F444W/F200W flux ratios for all 66 NIRCam sources. The median values for each group of sources, calculated from Bayesian bootstrapping (3000 iterations and  $1\sigma$  confidence), are shown as the black matching markers. Among the 37 newly identified JWST sources, the median F444W/F150W flux ratio is  $\sim 40\%$  higher than that of the 29 sources reported in DS07. The median F200W/F150W and F444W/F200W flux ratios of the JWST-detected sources are also 16% and 57% higher than

**Table 1**  
Source Photometry

| ID  | R.A.<br>(deg) (ICRS) | Decl.<br>(deg) (ICRS) | Dist. from<br>Center (kpc) | F150W<br>(mJy) | F200W<br>(mJy) | F335M<br>(mJy) | F444W<br>(mJy) | F560W<br>(mJy) | F770W<br>(mJy) | F1500W<br>(mJy) |
|-----|----------------------|-----------------------|----------------------------|----------------|----------------|----------------|----------------|----------------|----------------|-----------------|
| C1  | 345.814664           | 8.8737306             | 0.58                       | 0.26 ± 0.02    | 0.27 ± 0.02    | 0.22 ± 0.02    | 0.23 ± 0.02    | ...            | ...            | ...             |
| C2  | 345.8148249          | 8.874195              | 0.47                       | 0.14 ± 0.02    | 0.13 ± 0.01    | 0.17 ± 0.03    | 0.21 ± 0.02    | ...            | ...            | ...             |
| C3  | 345.8153678          | 8.8742908             | 0.54                       | 0.13 ± 0.02    | 0.14 ± 0.02    | 0.15 ± 0.02    | 0.13 ± 0.02    | ...            | ...            | ...             |
| C4  | 345.8148865          | 8.8735722             | 0.49                       | 0.14 ± 0.02    | 0.17 ± 0.02    | 0.19 ± 0.04    | 0.16 ± 0.02    | ...            | ...            | ...             |
| C5  | 345.8146074          | 8.8739447             | 0.60                       | 0.13 ± 0.01    | 0.14 ± 0.01    | 0.13 ± 0.01    | 0.12 ± 0.01    | ...            | ...            | ...             |
| N1  | 345.8149157          | 8.8736028             | 0.44                       | 0.11 ± 0.02    | 0.12 ± 0.03    | 0.18 ± 0.03    | 0.16 ± 0.02    | ...            | ...            | ...             |
| N2  | 345.8148628          | 8.8735086             | 0.57                       | 0.10 ± 0.01    | 0.10 ± 0.01    | 0.18 ± 0.02    | 0.26 ± 0.02    | ...            | ...            | ...             |
| N3  | 345.8152803          | 8.8742575             | 0.45                       | 0.07 ± 0.01    | 0.08 ± 0.02    | 0.08 ± 0.02    | <0.07          | ...            | ...            | ...             |
| N4  | 345.8147162          | 8.8740557             | 0.50                       | 0.07 ± 0.01    | 0.08 ± 0.02    | 0.13 ± 0.03    | 0.11 ± 0.02    | ...            | ...            | ...             |
| N5  | 345.8153949          | 8.8741989             | 0.48                       | 0.07 ± 0.02    | 0.11 ± 0.02    | 0.27 ± 0.03    | 0.44 ± 0.03    | ...            | ...            | ...             |
| ... | ...                  | ...                   | ...                        | ...            | ...            | ...            | ...            | ...            | ...            | ...             |
| N36 | 345.8145609          | 8.8736856             | 0.71                       | <0.02          | <0.04          | 0.09 ± 0.01    | 0.10 ± 0.02    | ...            | ...            | ...             |
| N37 | 345.8155022          | 8.8736348             | 0.59                       | <0.02          | <0.03          | 0.07 ± 0.02    | 0.09 ± 0.02    | ...            | ...            | ...             |
| P1  | 345.8153549          | 8.8737623             | 0.30                       | <0.03          | <0.02          | 0.09 ± 0.03    | <0.06          | ...            | ...            | ...             |
| P2  | 345.8152995          | 8.8737334             | 0.33                       | <0.02          | <0.03          | 0.09 ± 0.02    | <0.08          | ...            | ...            | ...             |
| M1  | 345.8146537          | 8.8736629             | 0.59                       | ...            | ...            | ...            | ...            | 3.3 ± 0.7      | 15.4 ± 2.9     | 33.9 ± 4.3      |
| M2  | 345.8153581          | 8.8742113             | 0.48                       | ...            | ...            | ...            | ...            | 3.2 ± 0.6      | 15.3 ± 1.7     | 47.1 ± 4.0      |
| M3  | 345.8149285          | 8.8743432             | 0.52                       | ...            | ...            | ...            | ...            | 2.7 ± 0.6      | 13.6 ± 2.8     | 26.6 ± 2.6      |
| M4  | 345.8148351          | 8.8735317             | 0.54                       | ...            | ...            | ...            | ...            | 2.5 ± 0.7      | 12.3 ± 2.0     | 32.5 ± 2.8      |
| ... | ...                  | ...                   | ...                        | ...            | ...            | ...            | ...            | ...            | ...            | ...             |
| M10 | 345.8154655          | 8.8736699             | 0.56                       | ...            | ...            | ...            | ...            | 1.3 ± 0.5      | 6.0 ± 0.8      | 13.6 ± 1.8      |
| M11 | 345.814734           | 8.8739304             | 0.39                       | ...            | ...            | ...            | ...            | 1.0 ± 0.4      | 6.0 ± 1.2      | 6.7 ± 3.6       |

**Note.** The distance for each source is measured from the central AGN. All flux densities are in units of mJy. Source labels are structured as follows: C—regions first identified by DS07, N—new regions identified in the F150W and F444W filters, P—new regions specifically identified in the NIRCcam/F335M filter, M—new MIRI/F560W-identified star-forming regions. HST-identified sources (C1-C30) are in order of decreasing HST 1.1  $\mu\text{m}$  flux as measured and presented in DS07. All other sources are in order of decreasing 1.5  $\mu\text{m}$  (NIRCcam) or 5.6  $\mu\text{m}$  (MIRI) flux density. Upper limits indicate the source flux is below the  $3\sigma$  detection threshold for that filter.

(This table is available in its entirety in machine-readable form.)

those of the HST-detected sources, respectively. In addition, of these 37 new sources, 28 show red colors (F200W/F150W > 1.1 or F444W/F200W > 2.5). However, there are some newly identified regions with blue NIR colors (F200W/F150W < 1.1 and F444W/F200W < 2.5) that are consistent with the colors of the intermediate-aged HST sample. These sources were previously missed by HST, either due to being below the detection limit or blended with other sources.

Due to the large range in the resolution of the NIRCcam filters used, we cross-convolved each NIRCcam image with the PSF of the other filters used in Figure 4 to bring the image pairs to a common resolution and verify the colors measured in Section 3. The photometric measurements of these convolved images were found to be consistent with those of the nonconvolved images, indicating our photometric calibrations are accurate.

## 5. Discussion

As previously mentioned, 28 of the newly discovered sources show redder NIR colors, F200W/F150W > 1.1 or F444W/F200W > 2.5, than the rest of the sample. To help explain these red colors, we plot in Figure 4 Yggdrasil single-stellar population (SSP) models<sup>36</sup> (Zackrisson et al. 2011), assuming a Kroupa initial mass function (Kroupa 2001) and solar metallicity. We include two models, where we altered the fraction of ionizing photons ( $f_{\text{cov}}$ ) that ionize the cloud from

50% to 100%. Comparing the colors of our sample to the SSP models, we find that all regions have extinction levels of  $A_V \sim 1$  or greater, which is consistent with the values reported in DS07.

We separate the DS07 sample into three groups, as determined by their SED fits: sources older than 5 Myr, younger than 5 Myr, and those where ages could not be determined. To roughly estimate the ages of the NIRCcam star-forming regions, we use their NIR colors, and compare them to those of the HST-identified regions with younger stellar populations (<5 Myr). The majority of these younger HST sources span a specific color space,  $1.1 < \text{F200W}/\text{F150W} < 1.2$  and  $0.9 < \text{F444W}/\text{F200W} < 1.6$ , and are redder than most of the other HST sources. The median F200W/F150W and F444W/F200W ratios of these HST-detected young sources are 7% and 35% higher than the intermediate-aged HST-detected sources. One of these young sources, C7, has a significantly lower F200W/F150W value than the rest, but it lacks HST photometry longwards of 1.1  $\mu\text{m}$ , which suggests that the inferred age for C7 may be inaccurate.

Most of the newly discovered JWST sources are redder in both colors than the young regions cataloged in DS07. Many of these sources are likely very young with significant dust obscuration and hot dust emission affecting their NIR colors. Some regions (N17, N20) fall close to the SSP models and thus likely contain a younger stellar population in a less obscured environment. Other regions (N14, N28) likely host younger stellar populations, but are highly obscured. Their colors can be

<sup>36</sup> <https://www.astro.uu.se/~ez/yggdrasil/yggdrasil.html>

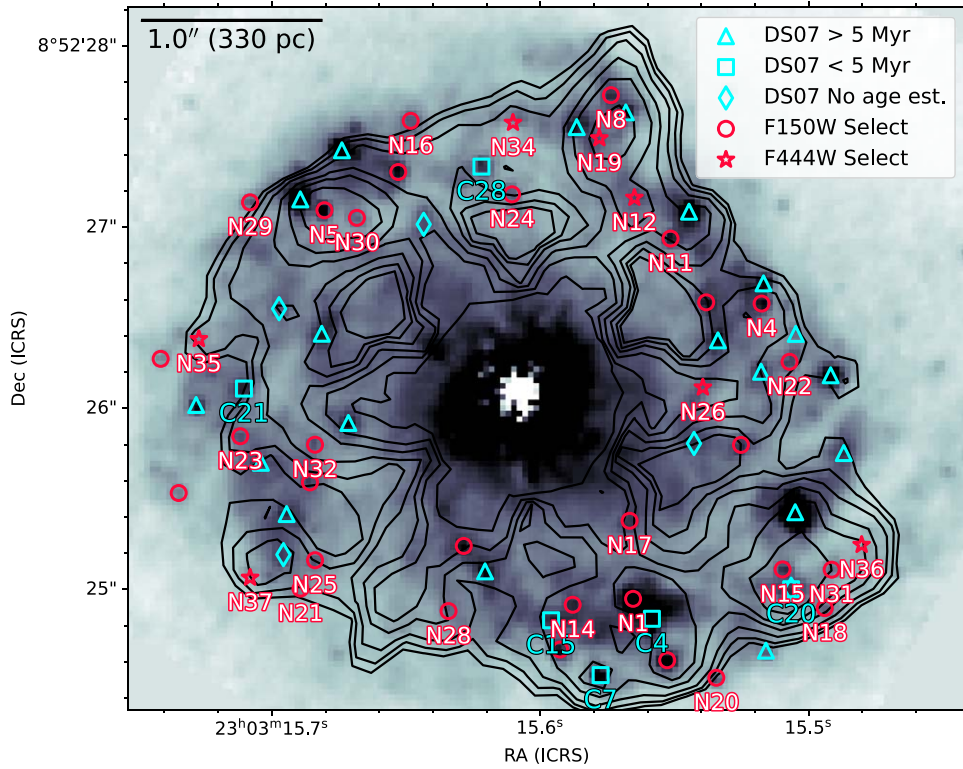


**Figure 3.** NIRCcam/F150W image where F150W-selected and NIRCcam/F444W-selected star-forming regions with red colors ( $F200W/F150W > 1.1$  or  $F444W/F200W > 2.5$ ) are labeled. The markers are the same as Figure 2 and the contour levels show the MIRI/F560W emission. Groups of sources with red NIR colors are somewhat clustered in the north and southwest regions, which coincide with the peaks of MIR and radio emission. The markers sizes are not representative of the extraction sizes.

mainly explained through varying degrees of attenuation, which can be as high as  $A_V \sim 7$ . They are also located within regions of strong MIR emission as shown in Figure 3. For the reddest sources,  $F444W/F200W > 2.5$ , heavy obscuration alone cannot explain the observed colors; a contribution of at least 25% from hot dust to the  $4.4 \mu\text{m}$  band is needed. The degree to which all these red sources are obscured can provide some further insight into the ages of the stellar populations. Timescales of stellar feedback in young clusters indicate the surrounding gas clouds can be expelled as fast as 2 Myr (Corbelli et al. 2017), or can take as long as 5 Myr (Messa et al. 2021). A progression of stellar ages has also been linked with obscuration, where younger populations (3 Myr) were shown to be more highly obscured than older populations (5 Myr; Hannon et al. 2019). This would suggest that the reddest sources in the starburst ring could be as young or younger than 3 Myr, which is consistent with the ages of dusty star-forming regions found in this work. Indeed, spectral fitting of MIRI/MRS data reveals that the detected sources are in some of the most obscured locations in the ring (Lai et al. 2022). In addition, star formation rates (SFRs) estimated via the  $\text{P}\alpha$ ,  $[\text{Ne II}]$ , and  $[\text{Ne III}]$  emission lines indicate that these regions have the highest SFRs in the ring. The 28 newly identified red sources account for  $\sim 6\%$  of the total luminosity of the starburst ring in the  $1.5 \mu\text{m}$  band and  $\sim 17\%$  in the  $4.4 \mu\text{m}$  band.

As mentioned in Section 4.1, radio observations have shown a molecular CO(3-2) gas bar oriented  $\sim 45^\circ$  north of east that connects the starburst ring through the center (Izumi et al. 2015). Comparison with the MIRI  $5.6 \mu\text{m}$  imaging reveals that the three strongest MIR emission regions (M1–M3) are cospatial with the radio peaks of the bar (D, B, C of Figure 6

in Izumi et al. 2015). These also coincide with the peak emission seen at 8.4 and 33 GHz (Oriente & Prieto 2010; Song et al. 2021). Analysis of the SEDs of these regions show a relatively steep spectral index ( $\sim 0.4\text{--}0.9$ ), suggesting a nonthermal origin (Oriente & Prieto 2010). Since about half of the HST and JWST-identified sources with younger ages in the northeast and southwest regions (N5, N15, N19, etc.) are aligned with these radio peaks, the origin of this nonthermal emission is most likely from supernovae events. If we assume the populations to be 3–5 Myr, then this emission could be from a second wave of OB stars.

Lastly, we note that seven of the red NIRCcam sources are located outside of the bar: six in the east/southeast (N21, N23, N25, N32, N35, N37) and five in the north/northwest (N4, N11, N12, N22, N26). In the north/northwest, the NIRCcam sources are located in the region of the CO(3-2) emission, which could be an extension of the bar (or a part of a spiral arm; Izumi et al. 2015, 2020). We also detect MIR emission at the same location (M3, M7, M8, M11). In the east/southeast, weak CO(2-1) and CO(3-2) emission that is cospatial with the east/southeastern sources is seen (Davies et al. 2004; Izumi et al. 2020). In addition, U et al. (2022) report  $[\text{Ar II}]$  strong emission that aligns well with the locations of our MIR sources. As such, these indicate a young stellar population and active star formation are occurring outside the bar.

## 6. Summary

In this Letter, we present JWST NIRCcam/SUB160P and MIRI/SUB128 multiband imaging of the circumnuclear starburst ring of NGC 7469. Our broadband imaging includes NIRCcam F150W, F200W, F335M, and F444W, and MIRI



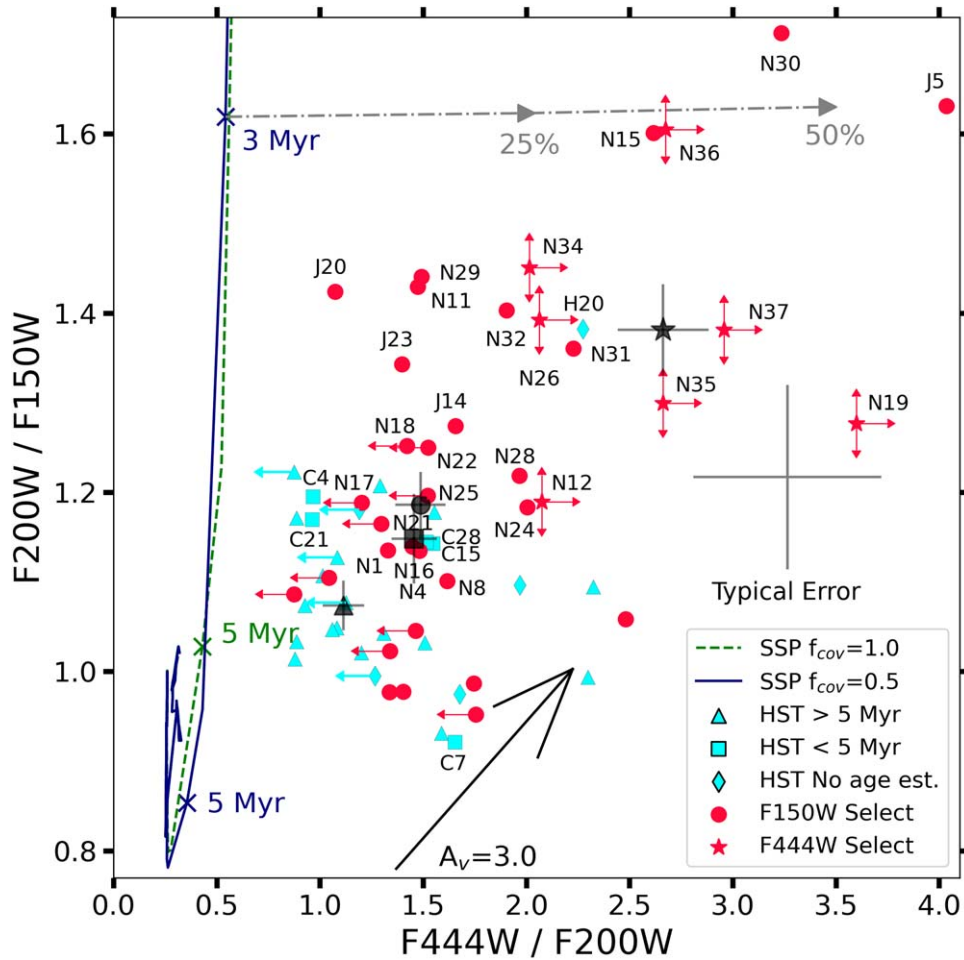


**Figure 4.** NIRCcam F200W/F150W vs. F444W/F200W color-color plot of the star-forming regions in the starburst ring of NGC 7469. The markers follow that of Figure 3, where red sources,  $F200W/F150W > 1.1$  or  $F444W/F200W > 2.5$ , are labeled. Sources with fluxes below the  $3\sigma$  detection threshold are treated as upper limits for the associated filter. The median colors of each source group are shown with the same markers, but in black. Two single-stellar population models (the green dashed line with  $f_{cov}$ , the fraction of ionizing photons, equal to 1.0 and the dark blue solid line with  $f_{cov} = 0.5$ ) are also shown, where the crosses denote the locations where the stellar age is 3 and 5 Myr. The typical error and an attenuation vector representing  $A_V = 3.0$  are included. The positions of the arrows indicate fractional contributions of 25% and 50% to the F444W flux. The majority of the JWST sources with red colors likely have young (3–5 Myr) stellar populations that are highly obscured and contain large amounts of hot dust.

F560W, F770W, and F1500W filters for a full wavelength coverage of 1.5–15  $\mu\text{m}$ . The significant improvement in sensitivity and resolution at NIR and MIR wavelengths has provided the most detailed look at the ages and colors of the star-forming regions in this starburst ring to date. The main results are as follows:

1. We report the detection of 59 star-forming regions in NIRCcam/F150W imaging and seven star-forming regions in NIRCcam/F444W, for a total of 66 detected regions. This more than doubles the 30 sources previously identified by HST. In addition, we detect 11 star-forming regions in the MIRI/F560W imaging.
2. Based on NIRCcam imaging, the new JWST-identified sources tend to be the reddest and faintest sources. Among these newly discovered regions, the median F444W/F150W flux ratio is about 40% higher than that of previously HST-identified regions. Their median F200W/F150W and F444W/F200W flux ratios are also higher by about 16% and 57%.
3. We compare SSP models to the NIR colors of the newly discovered sources to estimate their ages. We find that heavy dust obscuration and hot dust emission are

necessary to account for their red colors. Finally, we identify 28 star-forming regions with very red NIR colors that likely have young (<5 Myr) stellar populations. These sources account for  $\sim 6\%$  and  $\sim 17\%$  of the total luminosity of the starburst ring at 1.5 and 4.4  $\mu\text{m}$ , respectively. The 28 newly detected, young sources hidden by dust are a significant increase over the 4–5 young sources previously identified by HST.

4. The MIRI-selected regions contribute  $\sim 36\%$  of the total MIR emission of the starburst ring at 5.6  $\mu\text{m}$ . More than half of these regions lie within the previously known CO molecular bar. Most of the red NIRCcam-identified sources also fall within these MIR regions, indicating that with JWST we are discovering a large number of heavily obscured sources previously missed by HST.
5. The locations of three of the MIRI-selected regions agree well with the 8.4 and 33 GHz emission peaks found in the CO molecular bar. Since the origin of this emission is likely nonthermal, supernovae could be contributing significantly to the radio peaks. We also find four red NIRCcam sources in an east/southeastern CO emitting region that are likely not associated with the bar. These

regions could therefore be areas of active star formation that are off-axis from the bar.





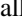








We thank the referee for the insightful feedback that helped improve the manuscript. The JWST data presented in this paper were obtained from the Mikulski Archive for Space Telescopes (MAST) at the Space Telescope Science Institute. The specific observations analyzed can be accessed at doi:10.17909/1ct2-x706. STScI is operated by the Association of Universities for Research in Astronomy, Inc., under NASA contract NAS5-26555. Support to MAST for these data is provided by the NASA Office of Space Science via grant NAG5-7584 and by other grants and contracts. This work is based on observations made with the NASA/ESA/CSA James Webb Space Telescope. These observations are associated with program 1328 and are supported by NASA grant ERS-01328. H.I. and T.B. acknowledge support from JSPS KAKENHI grant No. JP21H01129 and the Ito Foundation for Promotion of Science. Y.S. is supported by the NSF through grant AST 1816838 and the Grote Reber Fellowship Program administered by the Associated Universities, Inc./ National Radio Astronomy Observatory. The Flatiron Institute is supported by the Simons Foundation. V.U. acknowledges funding support from NASA Astrophysics Data Analysis Program (ADAP) grant 80NSSC20K0450. A.M.M. acknowledges support from the National Science Foundation under grant No. 2009416. S.A. gratefully acknowledges support from an ERC Advanced grant 789410, from the Swedish Research Council and from the Knut and Alice Wallenberg (KAW) foundation. K.I. acknowledges support by the Spanish MCIN under grant PID2019-105510GBC33/AEI/10.13039/501100011033. This work was also partly supported by the Spanish program Unidad de Excelencia María de Maeztu CEX2020-001058-M, financed by MCIN/AEI/10.13039/501100011033.

*Facilities:* JWST/NIRCam, JWST/MIRI, Spitzer/IRS, HST/NICMOS.

*Software:* GALFIT (Peng et al. 2010), WebbPSF (Perrin et al. 2014).

### ORCID iDs

Thomas Bohn  <https://orcid.org/0000-0002-4375-254X>  
 Hanae Inami  <https://orcid.org/0000-0003-4268-0393>  
 Tanio Diaz-Santos  <https://orcid.org/0000-0003-0699-6083>  
 Lee Armus  <https://orcid.org/0000-0003-3498-2973>  
 S. T. Linden  <https://orcid.org/0000-0002-1000-6081>  
 Vivian U  <https://orcid.org/0000-0002-1912-0024>  
 Jason Surace  <https://orcid.org/0000-0001-7291-0087>  
 Kirsten L. Larson  <https://orcid.org/0000-0003-3917-6460>  
 Aaron S. Evans  <https://orcid.org/0000-0003-2638-1334>  
 Thomas Lai  <https://orcid.org/0000-0001-8490-6632>  
 Yiqing Song  <https://orcid.org/0000-0002-3139-3041>  
 Joseph M. Mazzarella  <https://orcid.org/0000-0002-8204-8619>  
 Loreto Barcos-Munoz  <https://orcid.org/0000-0003-0057-8892>  
 Vassilis Charmandaris  <https://orcid.org/0000-0002-2688-1956>  
 Justin H. Howell  <https://orcid.org/0000-0001-6028-8059>  
 Anne M. Medling  <https://orcid.org/0000-0001-7421-2944>  
 George C. Privon  <https://orcid.org/0000-0003-3474-1125>  
 Jeffrey A. Rich  <https://orcid.org/0000-0002-5807-5078>  
 Sabrina Stierwalt  <https://orcid.org/0000-0002-2596-8531>

Susanne Aalto  <https://orcid.org/0000-0002-5828-7660>  
 Torsten Böker  <https://orcid.org/0000-0002-5666-7782>  
 Michael J. I. Brown  <https://orcid.org/0000-0002-1207-9137>  
 Kazushi Iwasawa  <https://orcid.org/0000-0002-4923-3281>  
 Matthew A. Malkan  <https://orcid.org/0000-0001-6919-1237>  
 Paul P. van der Werf  <https://orcid.org/0000-0001-5434-5942>  
 Philip Appleton  <https://orcid.org/0000-0002-7607-8766>  
 Christopher C. Hayward  <https://orcid.org/0000-0003-4073-3236>  
 Francisca Kemper  <https://orcid.org/0000-0003-2743-8240>  
 David Law  <https://orcid.org/0000-0002-9402-186X>  
 Jason Marshall  <https://orcid.org/0000-0001-7712-8465>  
 Eric J. Murphy  <https://orcid.org/0000-0001-7089-7325>  
 David Sanders  <https://orcid.org/0000-0002-1233-9998>

### References

- Armus, L., Mazzarella, J. M., Evans, A. S., et al. 2009, *PASP*, 121, 559  
 Behar, E., Peretz, U., Kriss, G. A., et al. 2017, *A&A*, 601, A17  
 Bouchet, P., García-Marín, M., Lagage, P. O., et al. 2015, *PASP*, 127, 612  
 Boyer, M. L., Anderson, J., Gennaro, M., et al. 2022, *RNAAS*, 6, 191  
 Bradley, L., Sipőcz, B., Robitaille, T., et al. 2022, *astropy/photutils*: 1.5.0, Zenodo, doi:10.5281/zenodo.6825092  
 Brown, G., & Gnedin, O. Y. 2021, *MNRAS*, 508, 5935  
 Corbelli, E., Braine, J., Bandiera, R., et al. 2017, *A&A*, 601, A146  
 Davies, R. I., Tacconi, L. J., & Genzel, R. 2004, *ApJ*, 602, 148  
 Díaz-Santos, T., Alonso-Herrero, A., Colina, L., Ryder, S. D., & Knapen, J. H. 2007, *ApJ*, 661, 149  
 Fathi, K., Izumi, T., Romeo, A. B., et al. 2015, *ApJL*, 806, L34  
 Genzel, R., Weitzel, L., Tacconi-Garman, L. E., et al. 1995, *ApJ*, 444, 129  
 Gordon, K. D., Chen, C. H., Anderson, R. E., et al. 2015, *PASP*, 127, 696  
 Greene, T. P., Chu, L., Egami, E., et al. 2016, *Proc. SPIE*, 9904, 99040E  
 Hannon, S., Lee, J. C., Whitmore, B. C., et al. 2019, *MNRAS*, 490, 4648  
 Inami, H., Armus, L., Charmandaris, V., et al. 2013, *ApJ*, 777, 156  
 Inami, H., Armus, L., Matsuhara, H., et al. 2018, *A&A*, 617, A130  
 Izumi, T., Kohno, K., Aalto, S., et al. 2015, *ApJ*, 811, 39  
 Izumi, T., Nguyen, D. D., Imanishi, M., et al. 2020, *ApJ*, 898, 75  
 Kroupa, P. 2001, *MNRAS*, 322, 231  
 Krumholz, M. R., McKee, C. F., & Bland-Hawthorn, J. 2019, *ARA&A*, 57, 227  
 Lai, T. S. Y., Armus, L., U. V., et al. 2022, arXiv:2209.06741  
 Landt, H., Bentz, M. C., Ward, M. J., et al. 2008, *ApJS*, 174, 282  
 Larson, K. L., Diaz-Santos, T., Armus, L., et al. 2020, *ApJ*, 888, 92  
 Linden, S. T., Evans, A. S., Rich, J., et al. 2017, *ApJ*, 843, 91  
 Linden, S. T., Song, Y., Evans, A. S., et al. 2019, *ApJ*, 881, 70  
 Lu, K., Wang, J., Zhang, Z., et al. 2021, *ApJ*, 918, 50  
 Messa, M., Calzetti, D., Adamo, A., et al. 2021, *ApJ*, 909, 121  
 Miles, J. W., Houck, J. R., & Hayward, T. L. 1994, *ApJL*, 425, L37  
 Müller-Sánchez, F., Prieto, M. A., Hicks, E. K. S., et al. 2011, *ApJ*, 739, 69  
 Norris, M. A., van de Ven, G., Kannappan, S. J., Schinnerer, E., & Leaman, R. 2019, *MNRAS*, 488, 5400  
 Orienti, M., & Prieto, M. A. 2010, *MNRAS*, 401, 2599  
 Peng, C. Y., Ho, L. C., Impey, C. D., & Rix, H. 2010, *AJ*, 139, 2097  
 Perrin, M. D., Sivaramakrishnan, A., Lajoie, C.-P., et al. 2014, *Proc. SPIE*, 9143, 91433X  
 Peterson, B. M., Grier, C. J., Horne, K., et al. 2014, *ApJ*, 795, 149  
 Ramos Almeida, C., Levenson, N. A., Alonso-Herrero, A., et al. 2011, *ApJ*, 731, 92  
 Rieke, G. H., Ressler, M. E., Morrison, J. E., et al. 2015, *PASP*, 127, 665  
 Robledo-Orus, A. C., Torres-Papaqui, J. P., Longinotti, A. L., et al. 2021, *ApJL*, 906, L6  
 Soifer, B. T., Bock, J. J., Marsh, K., et al. 2003, *AJ*, 126, 143  
 Song, Y., Linden, S. T., Evans, A. S., et al. 2021, *ApJ*, 916, 73  
 Stetson, P. B. 1987, *PASP*, 99, 191  
 Stierwalt, S., Armus, L., Surace, J. A., et al. 2013, *ApJS*, 206, 1  
 U, V., Lai, T., Bianchin, M., et al. 2022, *ApJL*, 940, L5  
 Xu, X., & Wang, J. 2022, *ApJ*, 933, 110  
 Zackrisson, E., Rydberg, C., Schaerer, D., Ostlin, G., & Tuli, M. 2011, *ApJ*, 740, 13